
















RESEARCH ARTICLE | SEPTEMBER 13 2022

A high-Q superconducting toroidal medium frequency detection system with a capacitively adjustable frequency range > 180 kHz

F. Völksen; J. A. Devlin ; M. J. Borchert; S. R. Erlewein; M. Fleck ; J. I. Jäger; B. M. Latacz ; P. Micke ; P. Nuschke; G. Umbrazunas ; E. J. Wursten ; F. Abbass; M. A. Bohman ; D. Popper; M. Wiesinger ; C. Will ; K. Blaum ; Y. Matsuda; A. Mooser; C. Ospelkaus ; C. Smorra ; A. Soter ; W. Quint; J. Walz; Y. Yamazaki ; S. Ulmer 



Rev Sci Instrum 93, 093303 (2022)
<https://doi.org/10.1063/5.0089182>



View
Online



Export
Citation

CrossMark

A high-Q superconducting toroidal medium frequency detection system with a capacitively adjustable frequency range >180 kHz

Cite as: *Rev. Sci. Instrum.* **93**, 093303 (2022); doi: [10.1063/5.0089182](https://doi.org/10.1063/5.0089182)

Submitted: 23 February 2022 • Accepted: 23 July 2022 •

Published Online: 13 September 2022



View Online



Export Citation



CrossMark

F. Völksen,^{1,2} J. A. Devlin,^{1,3,a)} M. J. Borchert,^{1,4,5} S. R. Erlewein,^{1,6} M. Fleck,^{1,7} J. I. Jäger,^{1,3,6} B. M. Latacz,^{1,6} P. Micke,^{1,3} P. Nuschke,^{1,4} G. Umbrazunas,^{1,8} E. J. Wursten,^{1,6} F. Abbass,⁹ M. A. Bohman,^{1,6} D. Popper,⁹ M. Wiesinger,⁶ C. Will,⁶ K. Blaum,⁶ Y. Matsuda,⁷ A. Mooser,⁶ C. Ospelkaus,^{4,5} C. Smorra,^{1,9} A. Soter,⁸ W. Quint,² J. Walz,^{9,10} Y. Yamazaki,¹ and S. Ulmer¹

AFFILIATIONS

¹RIKEN, Ulmer Fundamental Symmetries Laboratory, 2-1 Hirosawa, Wako, Saitama 351-0198, Japan

²GSI-Helmholtzzentrum für Schwerionenforschung GmbH, Planckstraße 1, D-64291 Darmstadt, Germany

³CERN, Esplanade des Particules 1, 1217 Meyrin, Switzerland

⁴Institut für Quantenoptik, Leibniz Universität, Welfengarten 1, D-30167 Hannover, Germany

⁵Physikalisch-Technische Bundesanstalt, Bundesallee 100, D-38116 Braunschweig, Germany

⁶Max-Planck-Institut für Kernphysik, Saupfercheckweg 1, D-69117 Heidelberg, Germany

⁷Graduate School of Arts and Sciences, University of Tokyo, 3-8-1 Komaba, Meguro, Tokyo 153-0041, Japan

⁸Eidgenössisch Technische Hochschule Zürich, Rämistrasse 101, 8092 Zürich, Switzerland

⁹Institut für Physik, Johannes Gutenberg-Universität, Staudinger Weg 7, D-55099 Mainz, Germany

¹⁰Helmholtz-Institut Mainz, Johannes Gutenberg-Universität, Staudingerweg 18, D-55128 Mainz, Germany

^{a)} Author to whom correspondence should be addressed: jack.alexander.devlin@cern.ch

ABSTRACT

We describe a newly developed polytetrafluoroethylene/copper capacitor driven by a cryogenic piezoelectric slip-stick stage and demonstrate with the chosen layout cryogenic capacitance tuning of ≈ 60 pF at ≈ 10 pF background capacitance. Connected to a highly sensitive superconducting toroidal LC circuit, we demonstrate tuning of the resonant frequency between 345 and 685 kHz, at quality factors $Q > 100\,000$. Connected to a cryogenic ultra low noise amplifier, a frequency tuning range between 520 and 710 kHz is reached, while quality factors $Q > 86\,000$ are achieved. This new device can be used as a versatile image current detector in high-precision Penning-trap experiments or as an LC-circuit-based haloscope detector to search for the conversion of axion-like dark matter to radio-frequency photons. This new development increases the sensitive detection bandwidth of our axion haloscope by a factor of ≈ 1000 .

© 2022 Author(s). All article content, except where otherwise noted, is licensed under a Creative Commons Attribution (CC BY) license (<http://creativecommons.org/licenses/by/4.0/>). <https://doi.org/10.1063/5.0089182>

Experiments at low energy with high fractional precision using the methods of atomic, molecular, and optical physics are an essential part of the search for physics beyond the Standard Model.¹ These include Penning-trap experiments, which provide ultra-precise measurements of fundamental constants^{2–5} as well as stringent tests of fundamental symmetries.^{6–10} Cryogenic Penning traps are typically used to measure the axial or modified cyclotron oscillation frequencies of the trapped particles using high-Q

resonant detectors.^{11,12} In a recent study,¹³ we showed that these resonant circuits, when placed in the strong magnetic field of a Penning-trap magnet, could also be used to constrain the coupling between light dark matter axion-like particles (ALPs) and photons. This allowed us to set narrow-band limits about one order of magnitude lower than other laboratory haloscopes.^{14–17} To this end, we used an axial detection circuit in the BASE experiment at CERN, in a narrow range of ALP masses between 2.7906 and 2.7914 neV, limited

by the detection bandwidth of the fixed-frequency resonator. Introducing a low-loss mechanism that provides broadband frequency tuneability at high signal detection sensitivity would enable us to investigate a wider range of ALP masses. Motivated by this application and the lack of technology that provides broadband tuneability of sensitive LC detection circuits operated in high magnetic fields, we have developed a polytetrafluorethylene (PTFE)/copper-based tunable cryogenic capacitor driven by a piezoelectric movable cryogenic stage, described in this manuscript. With this device, we can vary the resonance frequency of a superconducting LC-circuit between 345 and 685 kHz, while keeping its Q-value above 100 000. Connected to a cryogenic ultra-low-noise amplifier, $Q > 86\,000$ is reached in a frequency band between 520 and 710 kHz. This newly developed detector will extend the bandwidth of our ALP-photon conversion measurements by a factor of ≈ 1000 . Moreover, the device could also be used in a diverse range of high-precision Penning-trap studies, such as comparisons of particles with nearly identical masses¹⁸ and improved determinations of the proton mass in natural units.¹⁹ The resolution of some of these experiments is limited by an interplay of trap voltage tuning and residual magnetic field imperfections, as described in Ref. 6. The broadband high-Q tuning of the detector presented in this manuscript would allow measurements at constant trapping potentials for charge-to-mass (q/m) ratio differences >2 , eliminating this systematic limitation when comparing such greatly unequal masses. This device can also serve to extend the application of sympathetic cooling mediated by induced image currents of charged particles or ions through coolant ions stored in physically separated traps, extending what has been demonstrated with protons and beryllium ions,²⁰ as initially proposed in Ref. 21.

A schematic of the newly developed detection device is shown in Fig. 1. It consists of a superconducting parallel LC-circuit (the resonator) with capacitance C_p , inductance L , and effective parallel resistance $R_p = 2\pi\nu_0QL$. Here, Q and $\nu_0 = 1/(2\pi\sqrt{LC_p})$ are the quality factor and resonance frequency of the unloaded resonator, respectively. The resonance frequency can be varied via a tunable parallel-plate-type capacitor with capacitance C_T in parallel to the resonator. The adjusted resonance frequency is then

$\nu(C_T) = 1/(2\pi\sqrt{L(C_p + C_T)})$. A fraction of the voltage across the combined circuit is measured by an ultra-low-noise cryogenic GaAs field-effect transistor amplifier,²² operated at $T \approx 4$ K. The amplifier's output signal,

$$u_n = \sqrt{(4k_B T \text{Re}(Z(\nu))\kappa^2 + e_n^2)}, \quad (1)$$

is guided to room-temperature, processed by mixing stages, and analyzed with a Fast Fourier Transform (FFT) spectrum analyzer. Here, $\sqrt{4k_B T \text{Re}(Z(\nu))}$ is the thermal Johnson noise voltage of the combined impedance $Z(\nu)$ of the circuit, κ is an effective amplifier-to-resonator coupling factor,¹¹ and e_n is the equivalent input noise of the cryogenic amplification stage.

The superconducting resonator used in this work is similar to the device described in Ref. 11. It consists of an $N \approx 950$ -turn toroidal coil, made out of PTFE insulated NbTi wire with a conductive diameter of $75\ \mu\text{m}$, placed inside a cylindrical NbTi housing with an outer diameter of 48 mm and a length of 40 mm. Toroidal geometry is used for optimal flux-confinement, reducing radio-frequency losses induced in the housing by stray magnetic flux. We use superconducting NbTi wire, which is a type-II superconductor, with a critical magnetic field strength of $B_{c2} \approx 14.5$ T. This choice of material will enable us to place the detector in high magnetic fields,¹² which is necessary for the Penning-trap and axion-detection experiments we envision. The geometry of the toroid was optimized such that its cross-sectional area is maximized at the shortest length of superconducting wire, while considering the boundary conditions defined by geometrical constraints of the experiment. To keep the parasitic capacitance of the coil low, we use three-layer chamber windings. The individual chambers are machined onto the PTFE coil core, which shapes the toroid. The unloaded resonator has a resonance frequency $\nu_0 = 936.479(1)$ kHz and $Q = 197\,000(4000)$. Using an LCR meter and by investigating the change in the circuit's resonance frequency ν_0 with different parallel test capacitances C_T , we determine the inductance $L = 2.56(15)$ mH of the toroidal resonator. The capacitance of the unloaded system is $C_0 = 11.3(7)$ pF, out of which $2.3(1)$ pF can be attributed to a sapphire feedthrough used to thermalize the hot end of the toroidal coil.

The variable capacitance C_T is realized by changing the distance between two circular oxygen-free high conductivity (OFHC) copper plates, which are placed inside a grounded cylindrical OFHC copper housing with an outer diameter of 50 mm, an axial length of 51 mm, and a wall thickness of 2 mm. A sectional view of the capacitor is shown in Fig. 2(b). The fixed ≈ 4.5 mm thick "hot plate" of the capacitor is connected to one end of the resonator coil. A PTFE spacer with an axial length of 11 mm separates the hot plate from the closed side of the housing, reducing the parasitic capacitance. The spacer and the hot plate are held in place by brass screws with PTFE washers to prevent electrical contact. The second OFHC copper capacitor plate is joined with a brass screw to a cylindrical OFHC copper plunger, which can move axially inside the housing, and is guided by a low friction PTFE support in the lid of the capacitor housing. A spring washer is placed between the ground plate and plunger, which allows the two plates to align themselves when the plunger is fully inserted and the plates are pushed against each other. The corresponding screw was tightened enough to prevent measurable plate movement caused by the operation of the cryocooler. This movable plate is grounded by a copper braid to create

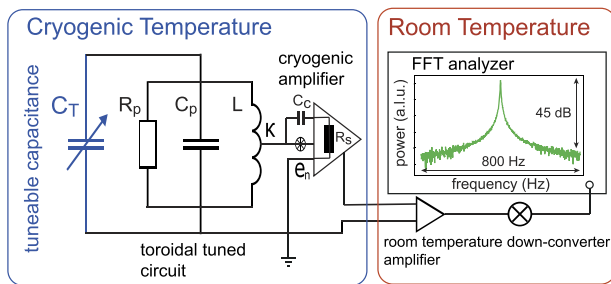


FIG. 1. Schematic of the superconducting LC detection system. The sensitive circuit is represented by the inductance L , capacitance C_p , and effective parallel resistance R_p . The tunable capacitor, shown in blue, is connected in parallel to the detector. A cryogenic amplifier is connected to the detector. The parasitic R_s and C_s are of interest for the later data interpretation. At room temperature, the signal is amplified by another stage, down-converted, and processed by a Fast Fourier Transform (FFT) spectrum analyzer. The spectrum shown on the FFT screen is representative of the measured data.

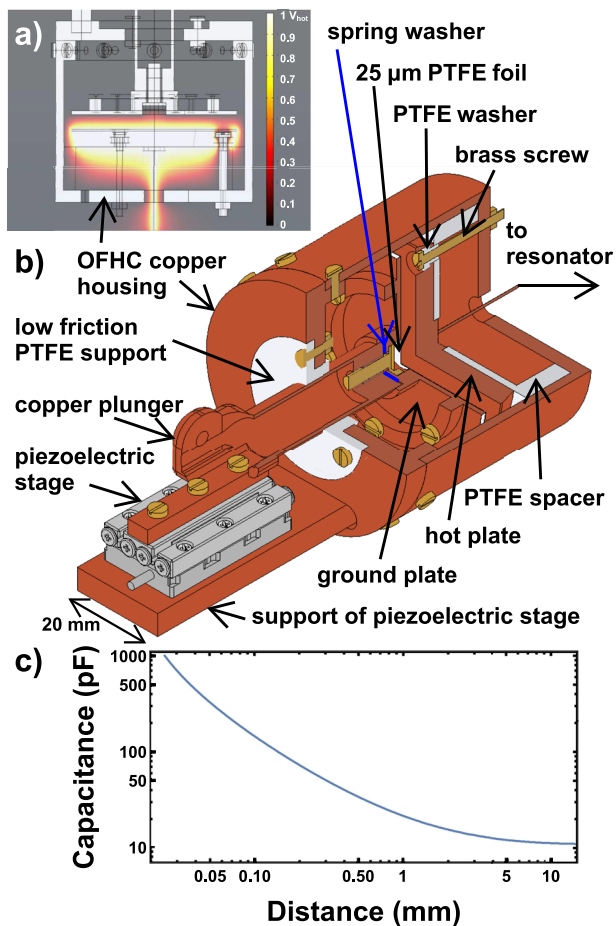


FIG. 2. (a) Finite element method (FEM) simulation of the electric potential inside the capacitor. (b) Sectional diagram of the cryogenic tunable capacitor. It should be noted that the copper braids connecting the ground plate with the resonator housing and the plunger to the ground would obscure other details and are omitted. (c) Simulation of the capacitance C_T as a function of distance.

a low-loss electrical connection. To avoid electrical contact between the plates when the plunger is fully inserted, a 25 μm PTFE film is placed on the movable plate, which also contributes additional capacitance due to the permittivity $\epsilon_{r,(PTFE)} \approx 2.1$. The position of the plunger is adjusted by a piezo-driven linear slip-stick stage, specified for operation in high magnetic fields, at cryogenic temperatures, and in ultra-high vacuum.²³ The piezoelectric stage is placed on a 5 mm thick OFHC copper plate that is directly thermally connected to the housing to thermalize it and avoid large thermal gradients. Additional thermalization is provided by the copper braid, which ensures that the plunger is connected to electrical ground. The stage can perform scan movements over a range of ≈ 2.6 μm by varying the voltage applied to the piezoelectric material. For the long-range slip-stick mechanism, a saw-tooth voltage ramp is applied to the crystal. The design allows the distance between the two plates to be varied between 25 μm and 14.4 mm, which is limited by the thickness of the PTFE foil and the space in the housing, respectively.

During the design of the cryogenic capacitor, careful consideration was given to the parasitic capacitance since this adds an unwanted reduction in the resonator frequency and limits the frequency tuning range, effectively increasing the value of C_p . A COMSOL Multiphysics simulation of the electrical field inside the final layout is shown in Fig. 2(a). From these simulations, we expect a total parasitic background capacitance of $C_p = 11.05$ pF and a maximum capacitance of 1001 pF for the fully inserted plunger, out of which 90% of the tuning range lies within the last 100 μm distance between both plates. Due to manufacturing tolerances, the actual experimental tuning range is expected to be lower. Figure 2(c) illustrates the capacitance based on the COMSOL simulation as a function of the distance between the respective plates, with 25 μm of the PTFE foil.

To characterize the tunable detector, we connect the hot plate of the capacitor (“to resonator” in Fig. 2) to the ungrounded end of the toroidal resonator (see Fig. 1)¹¹ and mount the assembly onto the 4 K stage of a Sumitomo SRDK-408D2 Gifford-McMahon cryocooler inside a vacuum chamber. Thermal shields connected to the first stage of the cooler surround the detector setup and shield the device from both 300 K thermal radiation and radio-frequency noise. Radio-frequency signals and DC-supply lines are guided to the detector via RF feedthroughs and low-thermal-conductivity wires.

We first characterize the cryogenic capacitor and resonator without the amplifier connected, as the input impedance of the amplifier reduces the Q-value of the combined resonator/capacitor, as discussed later in this manuscript. To this end, the input of the cooled connected resonator–capacitor system is weakly coupled to the active swept output port of a Rohde & Schwarz ZNC vector network analyzer (VNA) that excites the system. The synchronously swept input of the VNA is connected to the 1/4 decoupled tapped end of the coil, and the forward voltage gain S_{21} is recorded.²⁴

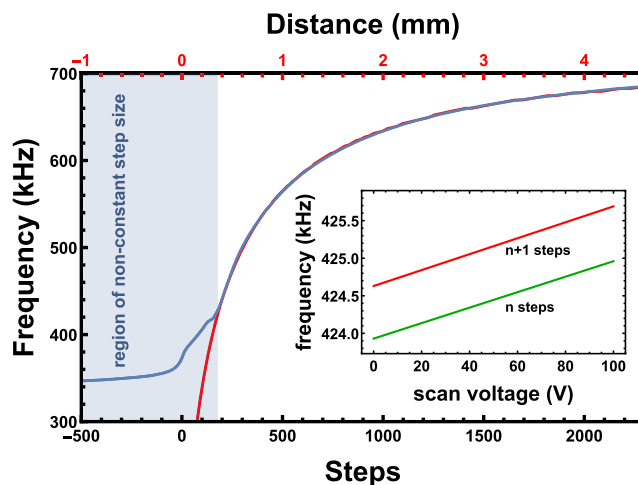


FIG. 3. The blue line shows the resonance frequency of the detector as a function of the steps of the piezoelectric drive. The red line is a fit based on the COMSOL simulation, assuming a step size of 2 μm. The inset shows two neighboring scan ranges, one step with minimum amplitude apart from another, to the frequency change by the step, confirming that there is no gap between neighboring scan ranges.

To ensure that analyzer and transmission line impedances do not impose limitations, both the radio-frequency excitation and the readout are decoupled via a <0.001 pF air capacitor network. The recorded forward voltage gain characteristics allow us to determine the frequency dependent resonator impedance $Z(\nu)$. Using power units, the 3 dB width of the recorded S_{21} transmission reflects the full-width at half maximum $\Delta\nu$ of the real part of the resonator impedance, from which the Q-value $Q = \nu_0/\Delta\nu$ of the tuned circuit is determined. This Q-determination approach is confirmed by exciting the LC circuit with radio-frequency pulses and recording time dependent ring-down signals of the excited device. From the recorded individual spectra, we extract the detector's resonance frequency $\nu(C_T)$ as a function of steps by the piezoelectric stage. The results are shown in Fig. 3. In the main plot, the blue line represents the measured resonance frequency, whereas the red curve is a numerical scaling fit of the COMSOL simulation results to the data. The abscissa gives the number of steps applied to the piezoelectric stage, while the upper red horizontal axis shows a calculation of the distance between the two plates, as inferred from the fit and the FEM simulations. Assuming a step size of $\approx 2 \mu\text{m}$ during the measurement brings data and simulation into the quantitative agreement. It should be noted that the step size itself is a function of applied voltage, temperature, and mechanical resistance. For distances of more than 0.4 mm between hot and grounded plates, the capacitance as a function of distance varies as expected. This behavior continues until the resonance frequency reaches 420 kHz, at which point the plates begin to touch, and the relationship between steps performed by the piezoelectric drive and distance moved is no longer constant, as the measured blue points diverge from the fit based on the simulation. Applying additional steps to the piezoelectric stage forces the plates closer together, and it is possible to reduce the resonance frequency to a minimum of ≈ 345 kHz. From this dataset, we determine a parasitic capacitance of the tunable capacitor of $C_p = 10.2(8)$ pF, which is in good agreement with the FEM simulation. The capacitive tuning range corresponding to the 340 kHz frequency tuning is $\Delta C_p = 58.2(6)$ pF and is limited by manufacturing tolerances of $\approx 100 \mu\text{m}$, which is consistent with our expectations of the current design. The quoted capacitance uncertainties, at the level <1 pF, are limited by small changes from cooldown to cooldown due to manufacturing tolerances in the mechanical and electrical assembly.

Additionally, we investigated whether the slip-stick motion provides continuous coverage of the entire frequency tuning span. To do this, we moved the ground plate close to the point at which it starts to touch the hot plate and scanned the frequency range between the frequencies corresponding to the maximum (100 V) and minimum (0 V) voltage applied to the piezoelectric stage. This gives the frequency tuning indicated by the green line in the inset of Fig. 3. Considering a single step with a minimum step amplitude of 36 V and repeating the 100 V voltage amplitude scan, we obtain the result indicated in red. As illustrated in the figure, the two scans overlap in frequency. Similar measurements were performed at different distances, confirming continuous frequency coverage over the entire tuning span of the device. The resolution of the device's DAC, in principle, allows fine tuning of the detector's resonance frequency to better than $100 \mu\text{Hz}$, a factor of >1000 smaller than observed drifts correlated with environmental changes such as laboratory temperature. The resolution of the frequency tuning of the detector is thus

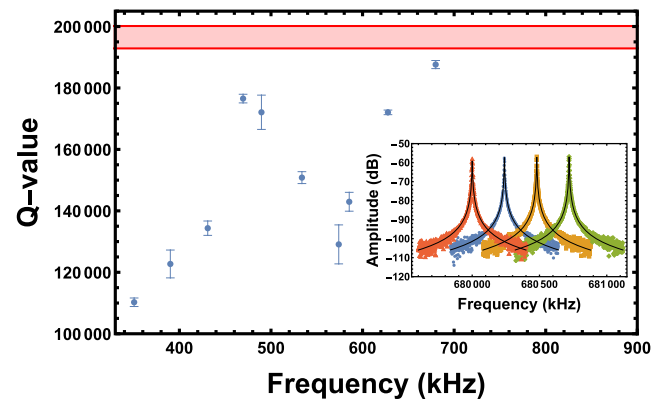


FIG. 4. Quality factor of the frequency tunable detector (without amplifier) as a function of the resonance frequency. Each point represents the average of 10 Q-value measurements determined from the measured S_{21} transmissions. The red area indicates the Q-value of the free resonator. Inset: Four frequency spectra for different positions of the hot plate of the cryogenic capacitor inside the housing.

not limited by the tuning capabilities of the cryogenic capacitor we have developed.

One of the most important measurements is the characterization of the detection sensitivity as a function of frequency. To study this, we measure the quality factor as a function of frequency, which is adjusted by the tunable capacitor. Figure 4 shows a broadband scan of the measured Q-values for different resonance frequencies. The inset shows four measured S_{21} transmissions of the device for resonance frequencies separated by 240 Hz intervals, a typical scan range for the use of such a device in an axion haloscope.¹³ The red horizontal band indicates the Q-value of the unloaded resonator. We first compare the residual series resistance $R_S = 2\pi\nu_0 L/Q$ of the unloaded resonator $R_{S,u} = 77(5)$ m Ω to the value obtained with the resonator connected to the tunable capacitor while it is adjusted close to its maximum separation ($\nu = 670$ kHz), resulting in $R_{S,c} = 58.3(3.4)$ m Ω . Comparing these two numbers, we see no detectable Q-value limitation imposed by the capacitor. Indeed, connecting the capacitor leads to a decrease of $\Delta R_S = 18(6)$ m Ω , which could be attributed to improved thermalization of the hot end of the resonator when connected to the thermalized copper plate of the capacitor, as also observed in other experiments carried out in our laboratory.

Figure 4 shows that the Q-value decreases as the frequency decreases; however, there is also a dispersive feature visible. The overall linear scaling of $Q(\nu)$ can be attributed to a frequency scaling $Q = 2\pi\nu L/R_S$ with a residual series resistance of $R_S = 73(5)$ m Ω , comparable to those of the high-performance resonators presented in Ref. 11. A detailed circuit analysis suggests that the dispersive feature is a consequence of either a predominantly capacitive coupling between the cold end of the resonant coil and ground in this particular cooldown or a result of parasitic coupling between the tap and an inductive element. Both the systematic investigation of these small residual series resistances and the understanding of the dispersive feature will be the subject of future work, with the goal to improve the quality of the superconductor-to-copper joints used on the detection coil¹¹ and to improve frequency matching and

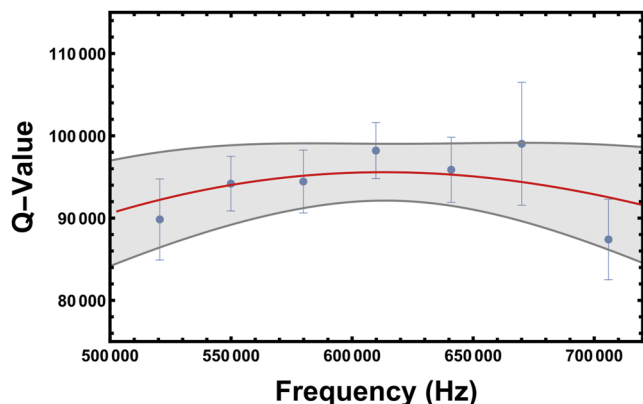


FIG. 5. Q-value of the capacitor combined with the superconducting resonator with an amplifier as a function of the resonance frequency. Each point represents the average of 10 Q-values determined by fitting the S_{12} spectra.

shielding of the rf-transmission lines. In summary, we can conclude that the losses imposed by the frequency tuning mechanism presented in this work are not detectable within the measurement uncertainties of our current setup.

To study the expected experimental performance when used as an axion haloscope antenna,¹³ we connect a cryogenic low-noise amplifier, similar to the devices used in Ref. 11, to a 1/4 tapped connection on the resonator coil, as shown in Fig. 1, and measure the voltage noise u_n on the output of the amplifier using a Rohde & Schwarz FSV A spectrum analyzer. Figure 5 shows the Q-value of the combined detector between 520 and 710 kHz. In this cooldown, an undesired mechanical interference blocked the last 200 μm of the tuning range; hence, in this measurement, the tuning range was smaller than in Fig. 4. In these measurements, the Q-value is reduced by the effective input resistance of the GaAs field-effect transistor input stage of the amplifier, which couples to the resonator and limits its quality factor.¹¹ Compared to the network analyzer data, no frequency dependent Q-value dispersion is observed, and the scaling of the Q-value as a function of frequency is strongly suppressed. This behavior is caused by the resonator/amplifier coupling. The dominant limiting mechanism arises from an effective parasitic capacitive coupling of the drain/source channel of the amplifier to the resonator, depicted in Fig. 1 by the IC intrinsic coupling capacitor C_C and the effective series resistance R_S of the drain-to-source channel. Given a constant background R_S , one would expect the Q-value to decrease linearly with frequency; however, so too should the Q-limiting series coupling of the resistance of the amplifier's drain-to-source channel. As a result, the effective system Q-value scales as

$$Q(\nu) = Q_0 \left(1 + \frac{(2\pi\nu)^4 C_C^2 L^2}{1 + (2\pi\nu)^2 C_C^2 R_S^2} \right)^{-1}, \quad (2)$$

which is the result of an algebraic analysis of the circuit shown in Fig. 1. This effective model is represented by the red solid line shown in Fig. 5, which is consistent with an effective capacitive-coupling-to-resistance ratio of $(C_C/R_S) = 80.7(6.4) \times 10^{-6}$ pF/ Ω . The gray solid lines indicate the 68% confidence interval on the best fit curve.

In conclusion, the device presented in this work allows the tuning of a high-Q resonant detection system by almost one frequency octave, without a significant reduction of its Q-value for the frequencies investigated. Connected to an ultra-low-noise amplifier, we observe $Q > 86\,000$ throughout the entire frequency range scanned in the measurement with the connected amplifier. To our knowledge, this is the first time that a device with such high detection sensitivity and large tuning bandwidth has been developed and characterized in the respective frequency range, which provides promising perspectives for its application in Penning-trap based determinations of fundamental constants^{6,7} and LC-circuit based axion haloscopes. Implemented into a dedicated axion detector and compared to the detection system used in Ref. 13, the Q-value of the new device would increase by a factor of ≈ 2 , while the tunable capacitor would extend the available frequency scan range by more than three orders of magnitude. An even larger tuning bandwidth at improved capacitive range linearity would be made available by using cryogenic cylindrical rotary capacitors; the development of such devices is currently under consideration.

ACKNOWLEDGMENTS

We acknowledge technical support by CERN, especially the Antiproton Decelerator operation group, CERN's cryolab team and engineering department, and all other CERN groups which provide support to Antiproton Decelerator experiments. We acknowledge financial support by RIKEN, the RIKEN EEE pioneering project funding, the RIKEN SPDR and JRA program, the Max-Planck Society, the European Union (FunI-832848, STEP-852818), CRC 1227 "DQmat" (DFG 274200144), the Cluster of Excellence "Quantum Frontiers" (DFG 390837967), the CERN fellowship program and the Helmholtz-Gemeinschaft. This work was supported by the Max-Planck, RIKEN, PTB-Center for Time, Constants, and Fundamental Symmetries (C-TCFS).

AUTHOR DECLARATIONS

Conflict of Interest

The authors have no conflicts to disclose.

Author Contributions

F. Völksen: Data curation (lead); Formal analysis (lead); Investigation (lead); Methodology (lead); Software (lead); Validation (lead); Visualization (lead); Writing – original draft (lead); Writing – review & editing (lead). **J. A. Devlin:** Conceptualization (lead); Data curation (lead); Formal analysis (lead); Investigation (supporting); Methodology (supporting); Software (lead); Supervision (lead); Visualization (lead); Writing – original draft (lead); Writing – review & editing (lead). **M. J. Borchert:** Methodology (supporting); Writing – review & editing (equal). **S. E. Erlewein:** Methodology (supporting); Software (supporting); Writing – review & editing (equal). **M. Fleck:** Software (supporting); Writing – review & editing (equal). **J. I. Jäger:** Writing – review & editing (equal). **B. M. Latacz:** Methodology (supporting); Software (supporting); Writing – review & editing (equal). **P. Mücke:** Writing – review & editing (equal). **P. Nuschke:** Writing – review &

editing (equal). **G. Umbrazunas**: Writing – review & editing (equal). **E. J. Wursten**: Writing – review & editing (equal). **F. Abbass**: Writing – review & editing (equal). **M. A. Bohman**: Writing – review & editing (equal). **D. Popper**: Writing – review & editing (equal). **M. Wiesinger**: Writing – review & editing (equal). **C. Will**: Writing – review & editing (equal). **K. Blaum**: Funding acquisition (supporting); Writing – review & editing (equal). **Y. Matsuda**: Funding acquisition (supporting); Writing – review & editing (equal). **A. Mooser**: Funding acquisition (supporting); Methodology (supporting); Writing – review & editing (equal). **C. Ospelkaus**: Funding acquisition (supporting); Writing – review & editing (equal). **C. Smorra**: Funding acquisition (supporting); Methodology (supporting); Software (supporting); Writing – review & editing (equal). **A. Soter**: Funding acquisition (supporting); Writing – review & editing (equal). **W. Quint**: Funding acquisition (supporting); Writing – review & editing (equal). **J. Walz**: Funding acquisition (supporting); Writing – review & editing (equal). **Y. Yamazaki**: Funding acquisition (supporting); Writing – review & editing (equal). **S. Ulmer**: Conceptualization (lead); Formal analysis (lead); Funding acquisition (lead); Investigation (supporting); Methodology (supporting); Project administration (lead); Resources (lead); Software (supporting); Supervision (lead); Visualization (lead); Writing – original draft (lead); Writing – review & editing (lead).

DATA AVAILABILITY

The data are available from the corresponding author on reasonable request.

REFERENCES

- ¹M. S. Safronova, D. Budker, D. DeMille, D. F. J. Kimball, A. Derevianko, and C. W. Clark, *Rev. Mod. Phys.* **90**, 025008 (2018).
- ²G. Schneider, A. Mooser, M. Bohman, N. Schön, J. Harrington, T. Higuchi, H. Nagahama, S. Sellner, C. Smorra, K. Blaum *et al.*, *Science* **358**, 1081 (2017).
- ³D. Hanneke, S. Fogwell, and G. Gabrielse, *Phys. Rev. Lett.* **100**, 120801 (2008).
- ⁴S. Sturm, F. Köhler, J. Zatorski, A. Wagner, Z. Harman, G. Werth, W. Quint, C. H. Keitel, and K. Blaum, *Nature* **506**, 467 (2014).
- ⁵R. X. Schüssler, H. Bekker, M. Braß, H. Cakir, J. R. Crespo López-Urrutia, M. Door, P. Filianin, Z. Harman, M. W. Haverkort, W. J. Huang *et al.*, *Nature* **581**, 42 (2020).
- ⁶S. Ulmer, C. Smorra, A. Mooser, K. Franke, H. Nagahama, G. Schneider, T. Higuchi, S. Van Gorp, K. Blaum, Y. Matsuda *et al.*, *Nature* **524**, 196 (2015).
- ⁷C. Smorra, S. Sellner, M. J. Borchert, J. A. Harrington, T. Higuchi, H. Nagahama, T. Tanaka, A. Mooser, G. Schneider, M. Bohman *et al.*, *Nature* **550**, 371 (2017).
- ⁸M. J. Borchert, J. A. Devlin, S. R. Erlewein, M. Fleck, J. A. Harrington, T. Higuchi, B. M. Latacz, F. Voelksen, E. J. Wursten, F. Abbass *et al.*, *Nature* **601**, 53 (2022).
- ⁹R. S. Van Dyck, Jr., P. B. Schwinberg, and H. G. Dehmelt, *Phys. Rev. Lett.* **59**, 26 (1987).
- ¹⁰E. G. Myers, *Atoms* **7**, 37 (2019).
- ¹¹H. Nagahama, G. Schneider, A. Mooser, C. Smorra, S. Sellner, J. Harrington, T. Higuchi, M. Borchert, T. Tanaka, M. Besirli *et al.*, *Rev. Sci. Instrum.* **87**, 113305 (2016).
- ¹²S. Ulmer, H. Kracke, K. Blaum, S. Kreim, A. Mooser, W. Quint, C. C. Rodegheri, and J. Walz, *Rev. Sci. Instrum.* **80**, 123302 (2009).
- ¹³J. A. Devlin, M. J. Borchert, S. Erlewein, M. Fleck, J. A. Harrington, B. Latacz, J. Warncke, E. Wursten, M. A. Bohman, A. H. Mooser *et al.*, *Phys. Rev. Lett.* **126**, 041301 (2021).
- ¹⁴N. Crisosto, P. Sikivie, N. S. Sullivan, D. B. Tanner, J. Yang, and G. Rybka, *Phys. Rev. Lett.* **124**, 241101 (2020).
- ¹⁵A. V. Gramolin, D. Aybas, D. Johnson, J. Adam, and A. O. Sushkov, *Nat. Phys.* **17**, 79 (2020).
- ¹⁶J. L. Ouellet, C. P. Salemi, J. W. Foster, R. Henning, Z. Bogorad, J. M. Conrad, J. A. Formaggio, Y. Kahn, J. Minervini, A. Radovinsky *et al.*, *Phys. Rev. Lett.* **122**, 121802 (2019).
- ¹⁷C. P. Salemi, J. W. Foster, J. L. Ouellet, A. Gavin, K. M. W. Pappas, S. Cheng, K. A. Richardson, R. Henning, Y. Kahn, R. Nguyen *et al.*, *Phys. Rev. Lett.* **127**, 081801 (2021).
- ¹⁸E. G. Myers, *Int. J. Mass Spectrom.* **349-350**, 107 (2013).
- ¹⁹F. Heiße, F. Köhler-Langes, S. Rau, J. Hou, S. Junck, A. Kracke, A. Mooser, W. Quint, S. Ulmer, G. Werth *et al.*, *Phys. Rev. Lett.* **119**, 033001 (2017).
- ²⁰M. Bohman, V. Grunhofer, C. Smorra, M. Wiesinger, C. Will, M. J. Borchert, J. A. Devlin, S. Erlewein, M. Fleck, S. Gavranovic *et al.*, *Nature* **596**, 514 (2021).
- ²¹D. J. Heinzen and D. J. Wineland, *Phys. Rev. A* **42**, 2977 (1990).
- ²²S. Ulmer, K. Blaum, H. Kracke, A. Mooser, W. Quint, C. C. Rodegheri, and J. Walz, *Nucl. Instrum. Methods Phys. Res., Sect. A* **705**, 55 (2013).
- ²³SmarAct, <https://www.smaract.com/linear-stages/product/slc-1730#specifications>, 2020.
- ²⁴R & S ZNC/ZND Vector Network Analyzers User Manual, 2019, p. 189.